Simultaneous observation of asymmetric speed-dependent capillary force hysteresis and slow relaxation of a suddenly stopped moving contact line

Dongshi Guan,[1] Yong Jian Wang,[1] Elisabeth Charlaix,[2] and Penger Tong[1]

[1]*Department of Physics, Hong Kong University of Science and Technology, Clear Water Bay, Kowloon, Hong Kong*

[2]*Laboratoire Interdisciplinaire de Physique, Université Joseph Fourier, 140 rue de la physique, F-38402 Grenoble, France*

(Received 11 February 2016; published 5 October 2016)

We report direct atomic-force-microscope measurements of capillary force hysteresis (CFH) and relaxation of a circular moving contact line (CL) formed on a long micron-sized hydrophobic fiber intersecting a liquid-air interface. By using eight different liquid interfaces with varying solid-liquid molecular interactions, we find a universal behavior of the asymmetric speed dependence of CFH and CL relaxation. A unified model based on force-assisted barrier crossing is used to connect the mesoscopic measurements of CFH and CL relaxation with the energy barrier height E_b and size λ associated with the surface defects. The experiment demonstrates that the CL pinning (relaxation) and depinning dynamics are closely related and can be described by a common microscopic framework.

DOI: 10.1103/PhysRevE.94.042802

I. INTRODUCTION

While liquid interfaces between two (immiscible) fluids are common in nature and industry, their motion over an ambient solid surface is complicated and not well understood, as the motion of the contact line between the liquid interface and solid surface is strongly influenced by the physical roughness and/or chemical heterogeneity on the solid surface. There are two outstanding problems associated with the three-phase contact line (CL), which have been with us for many years [1–5]. One is the moving contact line (MCL) problem, as it is incompatible with the nonslip boundary condition and would lead to unphysical infinite dissipation [6]. The other problem is contact angle hysteresis (CAH), where the contact line is pinned by the physical roughness and/or chemical heterogeneity on the solid surface, which causes the dynamic contact angle θ_i between the liquid and solid surfaces to depend on the direction of fluid motion [2], with the advancing contact angle θ_a being larger than the receding angle θ_r. Although considerable progress has been made recently in controlling the wettability of various textured solid surfaces [7,8], one still has a poor understanding of CAH on many ambient solid surfaces of interest [3].

The CL dynamics is known to be extremely sensitive to impurities and/or defects at both the liquid and solid interfaces. Previous experimental studies focused mainly on simple model systems with a single or a regular array of synthetic defects with sizes varying from milli- or micrometers [9–14] to nanometers [15–17]. While these experiments provided useful information about the CL dynamics at the single defect level, our understanding of CAH for many ambient surfaces, which have real-world features such as irregular overlapping defects at different length scales, is still limited. Understanding the interactions and dynamics of the CL is a fundamental issue in fluid physics and is also a concern of many industrial processes ranging from spreading of droplets, lubricants, and coatings to the extraction of oil from sandstone by injecting water or gas [4,5].

In a recent experiment [18], we used a newly developed hanging fiber probe [19] based on atomic force microscopy (AFM) to directly measure the capillary force acting on a CL. As shown in Fig. 1, the "long needle" AFM involves a vertical glass fiber of diameter d in the range 1–3 μm and length 150–200 μm, which is glued onto the front end of a rectangular cantilever beam. The other end of the fiber is immersed through a liquid-air interface, at which a circular CL is formed on the fiber surface. By moving the fiber up or down through the liquid interface at a constant speed u, the long needle AFM can accurately measure the capillary force $f_i(t)$ acting on the CL as a function of time t or traveling distance $s = ut$. Here $i = a$ indicates the advancing direction and $i = r$ indicates the receding direction. For a CL of length πd and contact angle θ_i with a liquid-air interface of surface tension γ, $f_i(t)$ can be written as [18,20–22],

$$f_i(t) = -\pi d\gamma \cos\theta_i(t), \tag{1}$$

where the sign of f_i is defined as $f_i \leqslant 0$ for $\theta_i \leqslant 90^\circ$ and $f_i > 0$ for $\theta_i > 90^\circ$.

In a recent letter [23], we reported an experimental study of capillary force hysteresis (CFH) observed on a hydrophobic fiber surface intersecting a water-air interface. In the experiment, the glass fiber was coated with a monolayer of Trichloro(1H,1H,2H,2H-perfluorooctyl) silane (FTS), and AFM was used to measure the advancing force f_a ($= -\pi d\gamma\cos\theta_a$) when the fiber was pushed downward and the receding force f_r ($= -\pi d\gamma\cos\theta_r$) when the fiber was pulled upward. It was found that the measured $f_r \neq f_a$ and shows an asymmetric speed dependence. This CFH reflected the fact that a different value of the unbalanced capillary force per unit length,

$$\Delta F_i \equiv \frac{|f_i - f_0|}{\pi d} = \gamma|\cos\theta_i - \cos\theta_0|, \tag{2}$$

is needed in order to depin the CL in the advancing and receding directions. Physically, ΔF_i can be viewed as a "rupture force" per unit length needed to break the "pinning bond" of the CL to the substrate, relative to the (unpinned) reference state $f_0 = -\pi d\gamma\cos\theta_0$ with θ_0 being the equilibrium contact angle.

A natural question regarding this work is, to what extent can the experimental results and theoretical analysis obtained in this particular system be applied to other wetting systems?

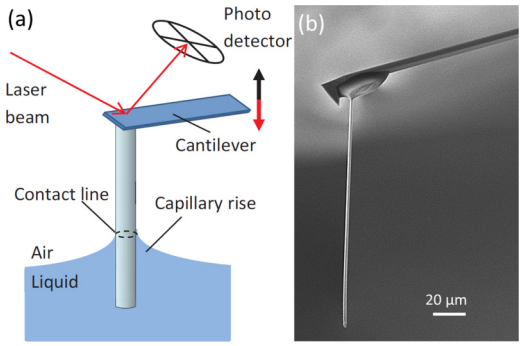

FIG. 1. (a) Sketch of the AFM-based capillary force apparatus at a liquid-air interface. (b) A scanning electron microscope image of the actual hanging glass fiber of diameter $d \simeq 2.2$ μm and length $l \simeq 150$ μm (partially adopted from Ref. [23]).

This is an important question because one wants to understand which aspects of the observed wetting properties are universal and which depend on the details of surface chemistry. Such an understanding is needed for a large number of practical problems involving various ambient solid surfaces and liquid interfaces including those coated with polymers, surfactants, and biomolecules (such as proteins and lipids). To answer this question, one needs to systematically change either the solid surface or liquid-air interface associated with the contact line.

In this paper, we report a detailed study of the speed-dependent CFH and relaxation of a MCL using the same FTS-coated glass fiber but with eight different liquid samples. By systematically varying the solid-liquid interactions with the different liquids, we find a universal behavior of the speed-dependent CFH and CL relaxation. The experiment demonstrates that the CL pinning (relaxation) and depinning dynamics are determined by a common microscopic mechanism, and the advancing and receding CLs are influenced by two different sets of relatively wetting and nonwetting defects on the surface. These two different types of defect landscapes give rise to an asymmetric speed dependence of CFH and two different metastable (pinned) states for MCL relaxation.

The remainder of the paper is organized as follows. We first describe the unified model based on force-assisted barrier crossing [24–26] for CL pinning and depinning in Sec. II. The experimental procedures and sample preparation methods are presented in Sec. III. The experimental results and further analysis and discussions are given, respectively, in Secs. IV and V. Finally, the work is summarized in Sec. VI.

II. THEORETICAL MODEL

A. Dynamic force spectroscopy for CL depinning

To model the depinning process of the CL, we consider a CL which is pinned by $N = (a/\lambda)\pi d$ defects, where a/λ is the defect line density with $a \leqslant 1$ being a numerical constant and λ a typical defect size. The average rupture force needed to break the pinning bound between the CL and a single defect is thus $\delta f_1 \simeq \pi d \Delta F/N = \Delta F(\lambda/a)$, where ΔF is given in Eq. (2). For the convenience of discussion, hereafter we drop the subscript i and use capital F for the quantities in units of force per length and lower case f for the quantities in units of

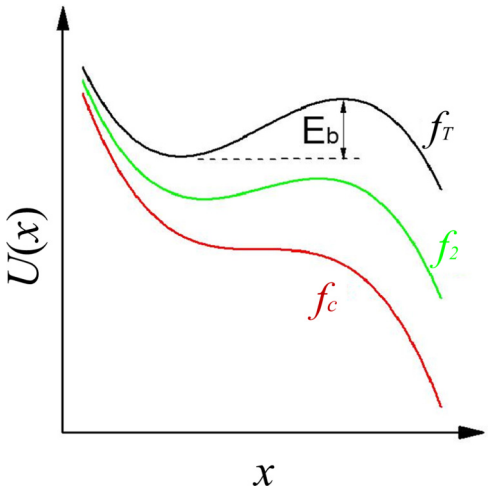

FIG. 2. Sketch of the linear-cubic potential $U(x)$ with three different characteristic forces: f_T (top black curve), $f_T < f_2 < f_c$ (middle green curve), and f_c (bottom red curve). The three curves are displaced vertically for clarity. The intrinsic barrier height E_b is shown for $\delta f = f_T$.

force. Some of the derivations to be given below have already been discussed in Ref. [23]. We include them here to fully explain the physical underpinning of the model.

The main effect of external pulling in the depinning process is to lower the energy barrier of the trapping (or blocking) potential $U_0(x)$ associated with the defect. Under a constant force δf, the effective potential becomes $U(x) = U_0(x) - \delta f x$. A simple linear-cubic potential of the form [27,28]

$$U(x) \simeq f_c x - \alpha(x - x_c)^3 \tag{3}$$

is often used to model the tilted potential $U(x)$ near the inflection point x_c of $U_0(x)$, which is given by $U_0''(x_c) = 0$ [24–26]. In the above, α is a constant proportional to $U_0'''(x_c)$, and f_c is the critical force at which the effective barrier to escape vanishes [24,25]. The value of f_c is given by the positive root of $f_c = U_0'(x_c)$.

Figure 2 shows a sketch of the linear-cubic potential $U(x)$ for three representative forces: $\delta f = f_T$ with $f_T = k_B T/\lambda$ being the thermal force associated with thermal energy $k_B T$ and defect size λ (top black curve), $f_T < \delta f = f_2 < f_c$ (middle green curve), and $\delta f = f_c$ (bottom red curve). As the force δf increases, the effective barrier height E_b^* decreases and vanishes at $\delta f = f_c$. As a result, the escape rate over the energy barrier E_b^* is increased and has the form [25,26]

$$K(\delta f) = K_0\sqrt{2}(1 - \delta f/f_c)^{1/2} e^{-E_b^*/k_B T}, \tag{4}$$

where K_0 is the attempt frequency, $E_b^* = E_b(1 - \delta f/f_c)^{3/2}$ is the effective energy barrier of $U(x)$ with E_b being the intrinsic energy barrier of $U_0(x)$, and $f_c = 3E_b/\lambda$ is the critical force.

Because the CL is pinned on the fiber surface, there is actually no relative motion between the CL and fiber surface when the fiber is initially pushed downward or pulled upward. The effect of fiber pulling at a constant speed u is to continuously stretch the liquid interface and thus produce a time-dependent elastic restoring force, $\delta f = k_s u t = \dot{f} t$, acting on the CL. Here $\dot{f} = k_s u$ is the loading rate with k_s being the spring constant of

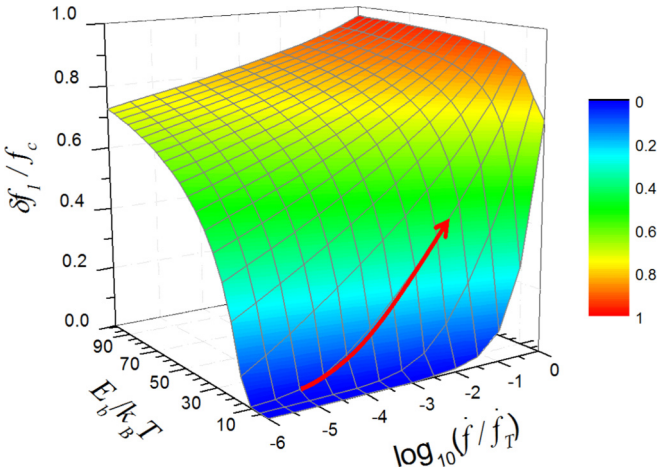

FIG. 3. 3D plot of the normalized rupture force $\delta f_1/f_c$ as a function of the normalized loading rate $\dot{f}/\dot{f}_T$ and intrinsic energy barrier E_b/k_BT, given in Eq. (5). The grid used on the surface plot shows increments of $\log_{10}(\dot{f}/\dot{f}_T) = 0.5$ and $E_b/k_BT = 5$, respectively. The red arrow indicates the variation of $\delta f_1/f_c$ with increasing $\dot{f}/\dot{f}_T$ for a fixed barrier $E_b/k_BT = 10$.

the liquid interface, which has been analytically calculated for a vertical thin fiber intersecting a liquid-air interface [18]. As the pulling force δf increases linearly with time t, the effective energy barrier $E_b^* = E_b(1 - \dot{f}t/f_c)^{3/2}$ continuously decreases and the escape rate $K(\delta f)$ increases. If the normalized loading rate $\dot{f}/f_c$ is much larger than the thermal activation rate $K(\delta f = 0)$ in Eq. (4), the force-assisted barrier crossing is determined primarily by the mechanical pulling without much help from thermal fluctuations. In this case, the rupture force needed is $\delta f_1 = f_c$. If $\dot{f}/f_c$ is smaller than $K(\delta f = 0)$, thermal fluctuations can help the barrier crossing and the rupture force needed is less than f_c.

For a single energy barrier E_b and size λ, one has [26]

$$\delta f_1 = f_c\left\{1 - \left[1 - \frac{k_BT}{E_b}e^X E_1(X)\right]^{2/3}\right\}, \tag{5}$$

where

$$X = \frac{2\dot{f}_T}{\dot{f}}e^{-E_b/(k_BT)} \tag{6}$$

and

$$E_1(X) = \int_X^\infty \frac{e^{-s}}{s}\,ds, \tag{7}$$

with $\dot{f}_T = k_BTK_0/\lambda = f_TK_0$ being the thermal rate. Note that $e^X E_1(X) \simeq \ln(1 + e^{-\alpha}/X)$ for small values of X [25,26], where $\alpha \simeq 0.577$ is the Euler constant.

Figure 3 shows a three-dimensional (3D) plot of the normalized rupture force $\delta f_1/f_c$ as a function of the normalized loading rate $\dot{f}/\dot{f}_T$ and intrinsic energy barrier E_b/k_BT, given in Eq. (5). The red arrow indicates the variation of $\delta f_1/f_c$ with increasing $\dot{f}/\dot{f}_T$ for a fixed barrier $E_b/k_BT = 10$. It is seen that for a fixed barrier E_b (and λ), $\delta f_1/f_c$ increases with $\dot{f}/\dot{f}_T$; the larger the value of $\dot{f}/\dot{f}_T$ is, the larger the rupture force δf_1 is needed to cross over the barrier. As mentioned above, by increasing $\dot{f}$ to a value closer to $\dot{f}_T$, thermal fluctuations play a less important role in barrier crossing, and thus the rupture force becomes closer to f_c. On the other hand, the $\dot{f}$ dependence (i.e., speed dependence) of $\delta f_1/f_c$ becomes weaker for a larger energy barrier E_b compared with k_BT. Figure 3 thus provide an overall view of the dynamic force spectroscopy for thermally activated barrier crossing [24].

Using Eq. (5), we find the depinning force ΔF of the CL [23]:

$$\Delta F \simeq \frac{a}{\lambda}f_c\left(1 - \left\{1 - \frac{k_BT}{E_b}\ln\left[1 + \frac{e^{-\alpha}(\dot{f}/\dot{f}_T)}{2e^{-E_b/k_BT}}\right]\right\}^{2/3}\right). \tag{8}$$

Equation (8) establishes a direct link between the macroscopically measurable quantity ΔF and the microscopic details of the defect, such as its effective energy barrier E_b and size λ. By varying the loading rate $\dot{f}$ (or pulling speed u), one can use the dynamic force spectroscopy to study the CL depinning. This method is particularly useful for such surfaces, on which E_b/k_BT is not very large (10–50 k_BT), and thus ΔF becomes more sensitive to the pulling speed u [29,30].

B. Equation of capillary force relaxation

To keep the CL moving on the fiber surface at a constant speed u (after it is depinned), an extra force is needed in order to overcome the extra dissipation introduced by the defects. This extra force is the unbalanced capillary force (per unit length) ΔF_i given in Eq. (2), which is created when the liquid interface near the CL changes its contact angle from θ_0 to θ_i. Once the motion of the CL is stopped, the (unbalanced) capillary force $f(t)$ will relax from its initial value $f(0) = f_a$ (or f_r) at $t = 0$ to its final value f_0 at large t. Physically, this relaxation process is accomplished by the CL moving along the fiber over a microscopic distance $z(t)$ with speed $u(t) = \dot{z}(t)$ back to its pinned state (minimum-energy state). With this understanding, the relaxation of $f(t) = k_sz(t)$ is just a reversal process of the CL depinning and can also be described by Eq. (8).

In the limit of $E_b/k_BT \gg 1$, Eq. (8) can be further simplified by a Taylor expansion and the final result has the Bell form [26,31],

$$\Delta F(t) \simeq \frac{2a}{\lambda}f_T\ln[1 + \beta\dot{z}(t)], \tag{9}$$

where $\beta = e^{-\alpha}k_s/[2\dot{f}_T\exp(-E_b/k_BT)]$ and $\Delta F(t) = \mp(k_sz(t) - f_0)/\pi d$. Here the "-" sign is used for advancing and "+" sign is for receding. This is a first-order ordinary differential equation about $z(t)$. In the limit $\beta\dot{z} \gg 1$, Eq. (9) can be rewritten as

$$\frac{dz(t)}{dt} = \frac{1}{\beta}\exp\left\{\frac{\mp[k_sz(t) - f_0]}{\pi d(2a/\lambda)f_T}\right\}. \tag{10}$$

The final solution of Eq. (10) is given by

$$f(t) = \mp\frac{2a\pi d}{\lambda}f_T\ln(\Gamma t + c) + f_0, \tag{11}$$

with the relaxation rate

$$\Gamma = \frac{K_0\exp(-E_b/k_BT)}{e^{-\alpha}\pi d(a/\lambda)}, \tag{12}$$

and the integration constant

$$c(u) = e^{\mp[f(0)-f_0]\lambda/(2a\pi d f_T)}, \quad (13)$$

which depends on the initial speed u via $f(0)$. Equation (11) uses the same set of parameters as those in Eq. (8) to describe the relaxation of $f(t)$.

III. EXPERIMENT

Details about the experimental apparatus and procedures as well as AFM operation have been described elsewhere [18,23], and here we mention only some key points.

A. Assembly of hanging fiber probe

The assembly of the hanging fiber probe is carried out under a high-magnification stereomicroscope using a motorized micromanipulator system. The thin glass fiber is pulled out of a capillary glass rod of diameter 1.0 mm using a pippette puller (P-97, Sutter Instrument). A UV-curable glue (Norland, NOA 81) is used to permanently connect the glass fiber to the front end of a rectangular cantilever beam. Commercial silicon micro-cantilevers with the spring constant $k_c \simeq 2.75$ N/m (FESP, no-coating, Bruker) are used in the experiment. After the assembling, the glass fiber probe is examined under a scanning electron microscope (SEM), and no visible defect is found on the fiber surface. The fiber diameter d is determined from the SEM image.

In the experiment, we use the glass fibers with diameter d in the range 1–3 μm and length 150–200 μm. The use of a micron-sized fiber provides a proper spatial average over the CL length πd for the study of the pinning-depinning dynamics of a MCL over a wide dynamic range. This mesoscale CL length is long enough to avoid seeing peculiar effects of a few individual defects but is short enough so that one can still observe large fluctuations in the measured capillary force. The use of a micron-sized fiber also ensures that the buoyancy force acting on the fiber is negligibly small ($\sim 10^{-2}$ nN). With the measured friction coefficient ξ of the long fiber [19,32], we find that the viscous drag force, $f_d = \xi u$, acting on the fiber with the speed u in the range studied here ($\sim 10^{-3}$ nN) is at least three orders of magnitude smaller than the measured capillary force. These features of the handing fiber probe are particularly useful for the study attempted here.

B. Surface treatments of glass fiber

After the assembly of the hanging fiber probe, the freshly prepared glass fiber is cleaned using a low vacuum plasma cleaner at the power 40 W for 15 min. After the plasma cleaning, the glass fiber is coated with a monolayer of trichloro(1H,1H,2H,2H-perfluorooctyl)silane (FTS), which is covalently grafted on the fiber surface, following the procedures given in Refs. [33,34]. A plastic dish containing a drop ($\sim$50 μl) of FTS solution (Aldrich) is put into a vacuum chamber together with the hanging fiber probe. The vacuum chamber is pumped with its pressure kept at 200 torr, and the FTS vapor coating lasts for 30 min. The sample is kept in the chamber for another 30 min after the pumping. The hanging fiber probe is then rinsed continuously with ethanol and water to remove the redundant FTS from the monolayer. The

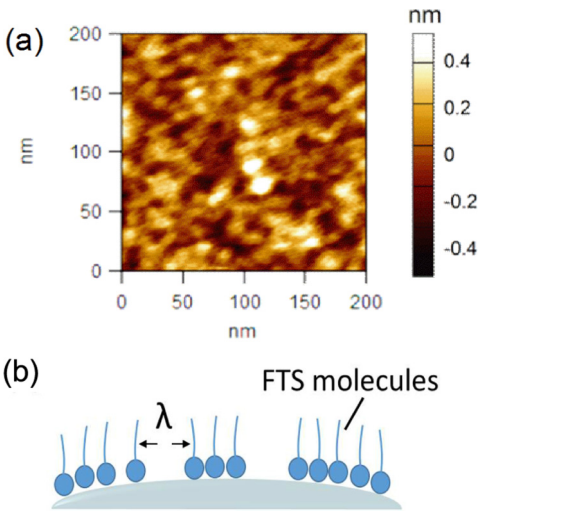

FIG. 4. (a) AFM topographic image of the top surface of a FTS-coated glass fiber in air. Typical height contrast is ± 0.4 nm. (b) Sketch of the FTS monolayer grafted on a glass fiber surface with defects of size λ (side view) (partially adopted from Ref. [23]).

FTS-coated glass surface is hydrophobic with an (advancing) contact angle $\sim 115^\circ$ for the water-air interface.

Figure 4(a) shows an AFM topographic image of the top surface of a FTS-coated glass fiber in air. The glass fiber was lying on a flat substrate during the AFM imaging. While the fiber surface is relatively smooth, it is nevertheless superimposed with a roughness landscape consisting of intertwined ridges (bright) and grooves (dark) of typical (symmetric) height $\sim$0.4 nm and domain size 20–50 nm. No obvious morphological change is observed for the glass fiber before and after the FTS coating, although the surface roughness with the FTS-coating is increased slightly from 0.15 nm to 0.17 nm. Because the FTS monolayer is only $\sim$1 nm in height, our AFM is unable to view the coating defects directly on a curved fiber surface.

Figure 4(b) shows a sketch of the FTS monolayer grafted on a glass fiber surface with defects of size λ (side view). The FTS chains are well organized in the monolayer, and they are densely packed and fully extended perpendicular to the substrate [33,34]. The FTS monolayer made by vapor-phase deposition is known to be more uniform and closely packed than all other self-assembled monolayers on the silica substrate [35–37]. For an FTS-coated glass surface, one usually can achieve 70%–90% of its maximum packing density [38], leaving uncovered holes on the otherwise hydrophobic surface, as sketched in Fig. 4(b). These uncovered holes are less hydrophobic compared with the uniform monolayer of FTS and thus become the main source of surface defects (see more discussions below). During the FTS coating, efforts are made to have a uniform coating as much as possible, by fine-tuning the vapor deposition conditions as described above, in order to reduce the number density of the coating defects.

C. Preparation of liquid interface

The liquid-air interface is prepared using a stainless steel well of 10 mm in diameter and 5 mm in depth. The well

TABLE I. Eight liquid samples used in the experiment and their literature values of viscosity η and surface tension γ. The values of the spring constant k_s of the liquid-air interface are obtained in the present experiment (see text for more details).

Liquids	η (cP)	γ (mN/m)	k_s (mN/m)
Octane (C_8H_{18})	0.508	21.14	14.42
Decane ($C_{10}H_{22}$)	0.838	23.37	17.11
Dodecane ($C_{12}H_{26}$)	1.383	24.91	17.66
Hexadecane($C_{16}H_{34}$)	3.032	27.05	20.32
Hexanol($C_6H_{13}OH$)	4.578	25.81	19.42
Octanol($C_8H_{17}OH$)	7.288	27.10	21.50
Water(H_2O)	1	72	65
FC77 (C_8F_{18})	1.3	13	-

has a sharp circular edge to pin the liquid-air interface in order to reduce unwanted surface flow. The stainless steel cell is mounted inside a closed AFM fluid cell. Prior to each measurement, the sample cell is thoroughly cleaned following the procedures as described in Ref. [19]. The entire fluid cell is sealed using a flexible rubber diaphragm to minimize the evaporation of the fluid during the experiment. The glass fiber in contact with the liquid is cleaned by ethanol prior to each measurement, to ensure that the force measurements are reproducible for different liquids. Because the FTS-coated fiber is hydrophobic with a very low surface energy, its surface properties remain stable and are not easily contaminated with repeated measurements.

The properties of the eight liquid samples used in the experiment are given in Table I. These liquids were chosen because their physical and chemical properties are stable, and a wide range of interfacial tensions are covered. Alkanes with carbon numbers 8 (octane), 10 (decane), 12 (dodecane), and 16 (hexadecane), respectively, are simple nonpolar liquids. Hexanol and octanol are primary alcohols, which have an extra hydroxyl (−OH) functional group at the end of a hydrocarbon chain, making them slightly polar than the alkanes. Water is a strong polar liquid. FC77 is a "fluorinated octane" with all the hydrogen atoms on the hydrocarbon chain being replaced by fluorine atoms. It is a strong nonpolar liquid with a molecular structure similar to that of the FTS molecules grafted on the fiber surface. Our goal here is to have a well-defined (reproducible and fixed) surface morphology and vary the solid-liquid interactions systematically with the eight different liquid samples. In this way, one can examine how the wetting properties change with a single experimental control parameter.

D. AFM operation

An AFM (MFP-3D, Asylum Research) operated under the contact mode is used to measure the capillary force $f(t)$. The entire AFM setup sits on an active vibration-isolation table, which is placed in an acoustic isolation hood (BCH-45, Asylum Research), further reducing the effect of surrounding vibrations. All the AFM measurements are conducted inside the hood at $24 \pm 0.5\,^{\circ}$C. The fiber speed u is accurately controlled by the z-axis piezoelectric actuator of the AFM in the range 0.5–100 μm/s with a travel distance s up to 25 μm. The spring constant k_c for each cantilever used is calibrated individually using the thermal power spectral density method [39]. Its value ($\simeq$2.75 N/m) is much larger than the spring constant k_s of the liquid interface. Typical vertical fluctuations (or noise level) of the modified cantilever are $\Delta\zeta \simeq 40$ pm. The force resolution is thus $k_c\Delta\zeta \simeq 0.1$ nN in the contact mode. The maximum force which can be measured with this AFM setup is about 700 nN. The capillary force measurements are conducted at a sampling rate of 2 kHz.

IV. EXPERIMENTAL RESULTS

A. Speed-dependent capillary force hysteresis

Figure 5 shows a typical hysteresis loop of the measured capillary force f when the FTS-coated glass fiber is pushed downward (advancing, A to C) and is pulled upward (receding, D to F) through a water-air interface. The zero point of this force measurement was calibrated with AFM when the fiber is in air before touching the liquid-air interface. In this case, no capillary force acts on the fiber. The fiber was then partially immersed in the water and the CL was pinned on the fiber surface. When the fiber advances, the pinned liquid interface is stretched, causing a linear increase in f with the distance traveled s, as shown by a straight line from A to B. When the restoring force becomes larger than a critical value, f_a ($= -\pi d\gamma\cos\theta_a$), the CL depins (at B) and begins a steady stick-and-slip motion, as evidenced by the horizontal fluctuations in the force curve from B to C. When the fiber is suddenly stopped at C, the measured $f(t)$ starts to relax with time t from C to D. When the direction of motion is reversed, a similar pinning-depinning process is repeated, as shown by the black receding curve from D to F. When the fiber is in contact with a liquid, $f = 0$ means the contact angle $\theta_i = 90^{\circ}$ [see Eq. (1)]. In this case, the capillary force has no vertical component parallel with the hanging fiber.

By varying the fiber speed u in the range 0.5–100 μm/s, we systematically measure the u dependence of the CFH loops for different liquid-air interfaces. This wide variation range of u is essential for the study of the u dependence of CFH. Figure 6 shows how the hysteresis loop of the measured f and corresponding contact angle θ_i [see Eq. (1)] change with increasing speed u. The measurements are made when the FTS-coated glass fiber is pushed downward (advancing) and

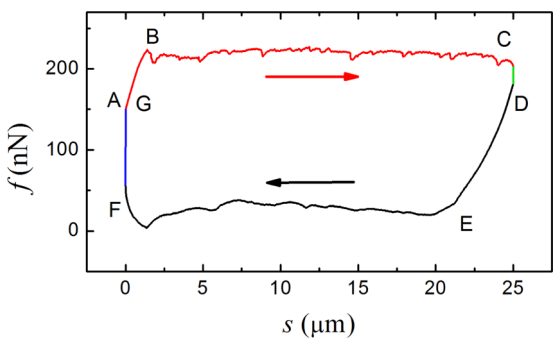

FIG. 5. Variations of the measured capillary force f as a function of traveling distance s when the FTS-coated glass fiber is pushed downward [advancing (→), A to C, red] and is pulled upward [receding (←), D to F, black]. The measurement is made at a water-air interface with the fiber speed u=10 μm/s.

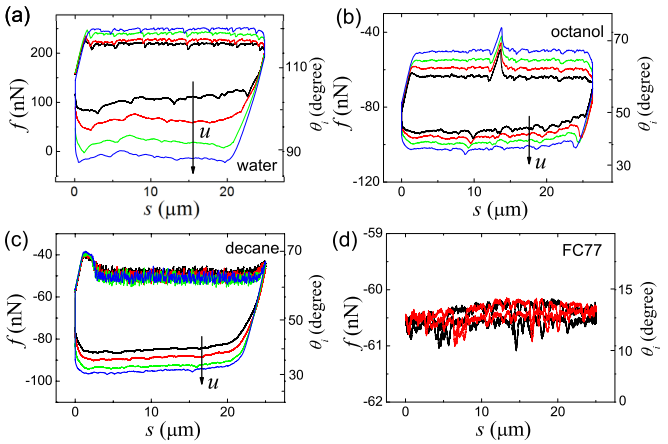

FIG. 6. Measured speed dependence of the hysteresis loop of the capillary force f and corresponding contact angle θ_i, when the FTS-coated glass fiber is pushed downward and is pulled upward through four different liquid-air interfaces: (a) water-air, (b) octanol-air, (c) decane-air, and (d) FC77-air. The measurements are made with fiber speed $u = 2$ μm/s (black), 5 μm/s (red), 20 μm/s (green), and 50 μm/s (blue), respectively. The black long arrow points the direction of increasing u.

upward (receding) through four different liquid-air interfaces: (a) water-air, (b) octanol-air, (c) decane-air, and (d) FC77-air. Except for FC77, all the other three interfaces in Fig. 6 show considerable u dependence in their CFH loops. Because the molecular structure of FC77 is very similar to that of FTS, the liquid-solid interfacial tension between FC77 and FTS is very small, and so do the CFH and its u dependence.

While the CFH for the three interfaces increases with u in general, each liquid interface has its own characteristic u dependence. (i) For the water-air interface, the u dependence of its CFH is asymmetric with the effect on the receding CL being much larger than that on the advancing CL, as discussed in Ref. [23]. (ii) For the octanol-air interface, on the other hand, the u dependence of its CFH is more symmetric with the effects in the advancing and receding directions being almost the same. A large spike of capillary force is observed in the steady-state advancing curve, which occurs at the same fiber position ($s \simeq 12$ μm), but does not show up in the receding curve. (iii) For the decane-air interface, its CFH loop shows an extreme case of asymmetric u dependence. The measured f and corresponding θ_i show u dependence only in the receding direction but not in the advancing direction. A small overshoot of f is observed at the beginning of the CL depinning in the advancing direction. The steady-state advancing curve also shows relatively large fluctuations compared with those in the receding curve.

The CFH loops shown in Fig. 6 are reproducible with little visible variation when the measurements are repeated either with the same push-down and pull-up cycles or with the reversing measurement cycles. We did not observe any systematic time dependence in the measured force curves during the experiment (typically l–3 h for one liquid). Note that with CFH the values of θ_a (and θ_r) obtained from Eq. (1) may not be necessarily the same as those obtained using the conventional photographic method, because the latter may

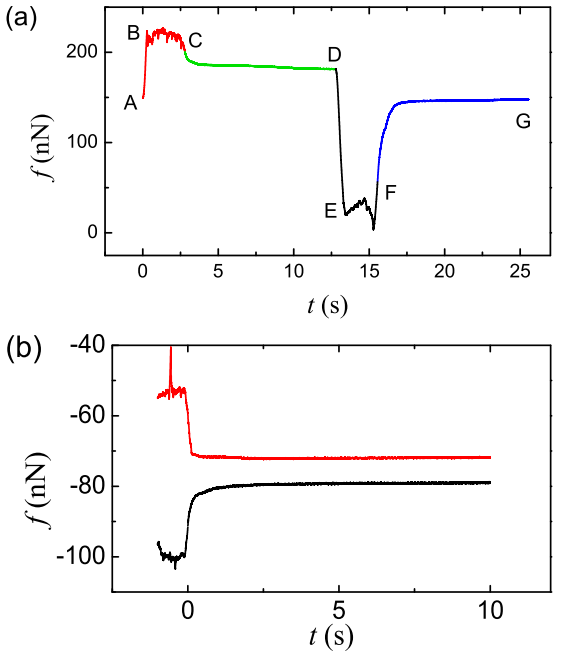

FIG. 7. (a) Replot of the same data shown in Fig. 5 as a function of time t when the fiber is pushed downward (advancing, A to C, red) and is pulled upward (receding, D to F, black). Curves C to D (green) and F to G (blue) show the relaxation of the measured $f(t)$ when the (moving) fiber is suddenly stopped at C and F, respectively, for 10 s. (b) Measured relaxation of the capillary force $f(t)$ when a MCL with speed $u = 20$ μm/s is suddenly stopped at $t = 0$. The measurements are made at the octanol-air interface in the advancing (red line) and receding (black line) directions.

depend sensitively on the distance away from the CL, at which the measurement is made [4]. Direct measurement of CFH at the CL does not have this experimental uncertainty. Figure 6 reveals a rich array of interesting behaviors of CFH and its u dependence for different liquid interfaces interacting with the FTS-coated glass fiber.

B. Relaxation of capillary force $f(t)$

Another interesting phenomenon observed for the FTS-coated fiber is the relaxation of capillary force $f(t)$ when a MCL is suddenly stopped. The measured $f(t)$ as a function of time t reveals the characteristic relaxation for each individual liquid interface. In Fig. 7(a) we replot the same hysteresis loop of the measured f in Fig. 5 in the time domain. It is seen that the measured $f(t)$ for the water-air interface relaxes smoothly to an asymptotic value $(f_0)_a$ in the advancing direction (C to D) and to a different asymptotic value $(f_0)_r$ in the receding direction (F to G). The relaxation of the measured $f(t)$ is asymmetric with its amplitude in the receding direction (F to G) being much larger than that in the advancing direction (C to D). In Fig. 7(b), we show the relaxation of $f(t)$ in the advancing (red line) and receding (black line) directions for the octanol-air interface. Before the MCL is stopped ($t < 0$), it undergoes stick-and-slip motion and the measured $f(t)$ shows steady-state fluctuations. After the MCL is stopped ($t > 0$), the measured $f(t)$ relaxes with t and reaches two

different asymptotic values $(f_0)_a$ and $(f_0)_r$, respectively, in the advancing and receding directions.

For the octanol-air interface, the relaxation in the two directions is approximately symmetric in both the decay rate and decay magnitude. For the decane-air interface, however, the relaxation in the two directions is strongly asymmetric with the measured $f(t)$ relaxing to $(f_0)_r$ only in the receding direction, and it does not change with t at all in the advancing direction (see more discussion in Sec. V C). By comparing the main features shown in Fig. 7 with those shown in Fig. 6, we find that the general behavior of the CL relaxation is closely connected to the u dependence of CFH. This finding further confirms that the two processes are determined by a common microscopic mechanism.

V. FURTHER ANALYSIS AND DISCUSSIONS

A. CFH and its origin

In the above, we have shown a rich array of interesting phenomena about the CL pinning (relaxation) and depinning dynamics. Hereafter we focus our attention on the speed dependence of the measured mean values of the advancing force f_a and receding force f_r and their relaxations. We recognize that the steady state fluctuations of the capillary force $f(t)$ may depend on details of the defect landscape and the dynamics of the CL as it sweeps over the fiber surface, which may involve such interesting dynamics as possible avalanche-like dynamics [40,41]. It is also of interest to know how the small overshoot in the advancing curve shown in Fig. 6(c) takes place at the decane-air interface. While these topics are important in their own right, they are beyond the scope of the present paper.

Before presenting the quantitative data, we first discuss some qualitative issues so that our data analysis is on firm ground. First, from the measurements shown in Fig. 6, it becomes clear that contact angle hysteresis (CAH) that was commonly reported in previous studies [1–5] is in fact a manifestation of capillary force hysteresis (CFH). To overcome the pinning potential imposed by the defects, an extra force ΔF_i [see Eq. (2)] is needed to depin the CL and keep it moving at a constant speed u. In the receding direction, the pulling of the fiber reduces the contact angle to θ_r and the resulting force $\Delta F_r = (f_r - f_0)/\pi d$ is increased [see Eq. (1)]. In the advancing direction, on the other hand, the pushing of the fiber increases the contact angle to θ_a, which also increases the force $\Delta F_a = (f_0 - f_a)/\pi d$. In this case, the hysteresis force can be written as [18]

$$f_h \equiv |f_a - f_r| = |(f_a - f_0) + (f_0 - f_r)| = \pi d(\Delta F_a + \Delta F_r). \quad (14)$$

As discussed in Sec. II, we model the CL depinning as a force-assisted barrier crossing process [25,26] without involving any bulk flow. This approach makes the comparison between the theory and experiment more accurate, compared with the measurement of the MCL speed, which often contains a significant contribution from the bulk flow [23].

Second, in many previous studies of CL dynamics, the equilibrium contact angle θ_0 is not known *a priori,* and one often estimates its value via the equation, $\cos\theta_0 \simeq (\cos\theta_a + \cos\theta_r)/2$ [18,20]. In writing Eqs. (2) and (14), we have assumed that the system has a common reference state, $f_0 = -\pi d\gamma \cos\theta_0$, so that both the advancing and receding CLs can relax to it. It is found from Figs. 6–7 that the pinning (relaxation) and depinning dynamics of the advancing CL is very different from that of the receding CL. They have different speed dependence and different asymptotic values of f_0, suggesting that the advancing and receding CLs have different pinned (metastable) states. Under this circumstance, the rupture force ΔF_i in Eq. (2) should be redefined as

$$\Delta F_i \equiv \frac{|f_i - (f_0)_i|}{\pi d} = \gamma|\cos\theta_i - \cos(\theta_0)_i|, \quad (15)$$

where f_i is the mean value of the measured capillary force at its steady state in the advancing ($i = a$, B to C) or receding ($i = r$, E to F) direction as shown in Fig. 5, and $(f_0)_i$ is the corresponding value after the relaxation (D and G) as shown in Fig. 7(a). Equation (15) will be used below for the data analysis.

Third, it was found in a recent experiment [18] that ambient solid surfaces often contain two types of coexisting and spatially intertwined defects with opposite natures. The two types of defects may be generated either by the positive and negative fluctuations of chemical heterogeneity relative to the mean or by the physical roughness of the surface with grooves and ridges. The CL is pinned primarily by the nonwetting (repulsive) defects in the advancing direction and by the wetting (attractive) defects in the receding direction. These two different types of defect landscapes, therefore, give rise to two different capillary forces f_a and f_r (or θ_a and θ_r) depending on the direction of the MCL. In principle, the magnitude of f_a and f_r and their speed dependence may depend on the nature and density of each set of the defects separately. The asymmetric behavior of CFH observed in Fig. 6 and the different asymptotic values $(f_0)_i$ as shown in Fig. 7(a) thus provide further supports to the "composite model". Only when the distribution of the two sets of defects is symmetric, one has $\Delta F_a \simeq \Delta F_r$ and one can use a common reference state f_0 (or θ_0) to characterize CFH, as shown in Eq. (14).

Finally, for an FTS-coated fiber, a uniform monolayer of FTS should be treated as a reference state without any defect. As sketched in Fig. 4(b), the uncovered holes on the otherwise uniformly coated surface serve as wetting defects. The nonwetting defects, on the other hand, may result from the local FTS spots with a higher density than the average. Such FTS spots may come from the remaining FTS residuals on the coated surface or from those rough surface spots with a higher density of FTS. Because the FTS-coated fiber surface has more wetting defects, the CL is pinned predominantly in the receding direction. This explains qualitatively why the observed u dependence of CFH and CL relaxation is asymmetric with the effect on the receding CL being much larger than that on the advancing CL.

Furthermore, the coating of a monolayer of FTS on the glass fiber surface converts the surface to a low-energy (hydrophobic) surface and thus reduces the overall energy scale of the defect landscape. While the mean and root-mean-squared values of surface energy can be uncorrelated in principle, they might also be correlated for the actual surfaces. We are aware of only two cases, in which the speed-dependent

CFH was observed. One is the liquid hydrogen meniscus on a solid cesium substrate at low temperatures (∼15 °K) [30]. Because of low temperature, all the interfacial tensions in the system are reduced to be very low. The other case is the FTS-coated fiber surface used in the present study. In these two cases, both the mean surface energy and the obtained values of the energy barrier are low (to have the speed dependence). We did not observe any u dependence in the measured CFH for the bare glass fiber [18], which is a high-energy surface. Even for an FTS-coated fiber surface, its defect landscape still has a range of energy barriers E_b/k_BT. Some of them are small so that they can only pin the CL temporally for a short period of time, and thermal fluctuations will help the CL to overcome the small pinning barriers and reach a metastable state having large pinning barriers with long lifetimes. These large pinning barriers prevent the CL from further relaxing to a global minimum energy state with a common capillary force f_0 and give rise to two different metastable states in the advancing and receding directions, respectively, with capillary forces $(f_0)_a$ and $(f_0)_r$.

B. Rupture force spectroscopy of CL depinning

With the above understanding, we now present the quantitative date. Figure 8(a) shows the measured depinning force ΔF_r of the receding CL as a function of fiber speed u for eight liquid samples used in the experiment. The measured ΔF_r all increases with u with an approximate $\ln u$ dependence. Water is found to have the largest value of ΔF_r while FC77 has the smallest value of ΔF_r with all other fluids in the middle between the two limiting cases. The three solid lines show, respectively, the fits to Eq. (8) for water (black line), octanol (blue line), and hexanol (red line). To display the fitting to other sets of data more clearly, we show, in Fig. 8(b), the magnified

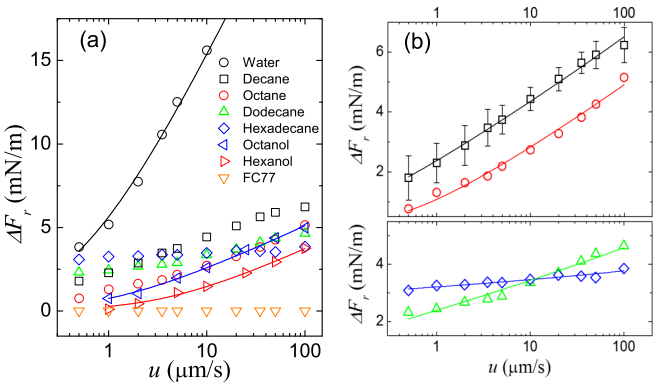

FIG. 8. (a) Measured depinning force ΔF_r for the receding CL as a function of fiber speed u for eight liquid samples: water (black circles), decane (black squares), octane (red circles), dodecane (green up triangles), hexadecane (blue diamonds), octanol (blue left triangles), hexanol (red right triangles), and FC77 (orange down triangles). The three solid lines show, respectively, the fits to Eq. (8) for water (black line), octanol (blue line), and hexanol (red line). (b) Magnified plots of the measured ΔF_r for alkanes: decane (black squares), octane (red circles), dodecane (green triangles), and hexadecane (blue diamonds). The error bars show the standard deviation of the measurements. The solid lines are the fits to Eq. (8).

plots of the measured ΔF_r for alkanes together with the fitting to Eq. (8). The measured ΔF_r varies slightly when different segments of the same fiber are used. In Fig. 8 we show the mean value of ΔF_r obtained using different segments of the same fiber. The error bars in Fig. 8(b) show the standard deviations of the measurements.

In the fitting, the energy barrier E_b and size λ are used as two fitting parameters. The value of other parameters in Eq. (8), including the defect line density parameter a, spring contact k_s of the liquid interface, and attempt frequency K_0, has been predetermined in the experiment. The value of k_s for each liquid-air interface is obtained directly from the slop of the linear increase of the measured f with the traveling distance s, as shown in Fig. 6 [18]. The measured values of k_s for the seven liquid-air interfaces used in the experiment are given in Table I. The attempt frequency K_0 is estimated as $K_0 \simeq 2D_0/\lambda^2 = 2k_BT/(\lambda^2\xi)$, where $D_0 = k_BT/\xi$ is the diffusion coefficient of the CL with $\xi = (1.1 \pm 0.3)\eta\lambda$ being its friction coefficient [42,43]. Here η is the viscosity of the liquid.

As mentioned above, for an FTS-coated glass surface, one usually can achieve 70%–90% of its maximum packing density [38]. We therefore choose $a = 0.3$ for both the advancing and receding cases, assuming that 30% of the CL length is occupied by the "uncovered holes," as sketched in Fig. 4(b). In previous studies of the speed-dependent wetting dynamics [44], $a = 1$ was used for simplicity. It is seen from Fig. 8 that all the data are well described by Eq. (8) (solid lines) and the final fitting results for different liquid samples are given in Table II.

Figure 9 shows the measured depinning force ΔF_a for the advancing CL as a function of fiber speed u for three liquid samples: water, octanol, and hexanol. Again, the measured ΔF_a all increases with u with an approximate $\ln u$ dependence. Water is found to have the largest value of ΔF_a while hexanol has the smallest value of ΔF_a with octanol in the middle between the water and hexanol. All the data are well described by Eq. (8) (solid lines) and the final fitting results are given in Table II.

C. Capillary force relaxation spectroscopy

As mentioned in Sec. II B, the relaxation of the capillary force $f(t)$ is a reversal process of the CL depinning and can be described by Eq. (11). Figure 10 shows the relaxation of the measured $f(t)$ and corresponding contact angle $\theta_i(t)$ as a function of time t after a MCL is suddenly stopped at $t = 0$. In the experiment, we measure $f(t)$ with 10 different values of the initial speed u in the range 0.5–100 μm/s. Figure 10 shows the plots with four typical values of u for the decane-air interface. It is seen that the measured $f(t)$ [or $\theta_i(t)$] does not change much in the advancing direction (upper four curves) for all the fiber speeds studied, but changes considerably in the receding direction (lower four curves). The decay rate of $f(t)$ in the receding direction depends sensitively on u, whereas the asymptotic value $(f_0)_r$ that the measured $f(t)$ relaxes to does not change much with u. The receding asymptotic value $(f_0)_r$, however, differs from the advancing asymptotic value $(f_0)_a$. The solid lines in Fig. 10 show the fits to Eq. (11) with E_b and λ as two fitting parameters. The value of other parameters in Eq. (11) is kept the same as that used in Fig. 8. To show the solid lines more clearly, the number of the data

TABLE II. Fitted values of energy barrier E_b, size λ, and critical force $f_c = 3E_b/\lambda$ in the advancing (adv.) and receding (rec.) directions. The values of E_b and λ are obtained using both the rupture force spectroscopy and capillary force relaxation spectroscopy. The experimental uncertainties in the rupture force spectroscopy result mainly from those in the attempt frequency K_0 and defect line density parameter a. The error bars in the capillary force relaxation spectroscopy indicate the standard deviation of the measurements under different initial fiber speeds u (see text for more details).

	Rupture force spectroscopy			Capillary force relaxation spectroscopy		
Liquids	E_b ($\pm 0.7 k_BT$) adv./rec.	λ ($\pm$0.3nm) adv./rec.	f_c (k_BT/nm) adv./rec.	E_b (k_BT) adv./rec.	λ (nm) adv./rec.	f_c (k_BT/nm) adv./rec.
Octane	/15.3	/1.74	/26.38	$/14.9 \pm 2.2$	$/1.64 \pm 0.49$	/27.26
Decane	/16.4	/1.76	/27.95	$/16.9 \pm 0.8$	$/1.63 \pm 0.27$	/31.10
Dodecane	/17.4	/2.54	/20.55	$/16.4 \pm 1.4$	$/2.45 \pm 0.35$	/20.55
Hexadecane	/55.3	/6.97	/23.80	$/40.6 \pm 6.1$	$/4.77 \pm 1.43$	/25.53
Hexanol	10.4/10.5	1.29/1.57	24.19/20.06	$10.7 \pm 0.9/11.8 \pm 0.9$	$1.67 \pm 0.35/1.58 \pm 0.30$	19.22/22.40
Octanol	11.6/11.8	1.33/1.58	26.10/22.31	$11.9 \pm 0.7/12.3 \pm 0.8$	$1.33 \pm 0.25/1.76 \pm 0.35$	26.84/21.00
Water	14.6/16.8	1.30/0.73	33.05/67.40	$15.4 \pm 0.9/16.8 \pm 0.8$	$1.41 \pm 0.28/0.76 \pm 0.14$	32.77/66.32

points in the range of delay time 0.01–10 s is reduced. It is seen that Eq. (11) fits the data well over four decades of decay time t, until the measured $f(t)$ reaches its asymptotic value $(f_0)_r$ at the long decay time ($t \simeq 10$ s). From the fittings with 10 different values of u, we obtain the mean values of $(E_b)_r = 16.9 \pm 0.8 k_BT$ and $\lambda_r = 1.63 \pm 0.27$ nm. The error bars quoted here are the standard deviations of the fitting results with 10 different speeds.

Similarly, we repeat the measurements of the capillary force relaxation with varying fiber speed u in the receding and advancing directions for all the seven liquid samples. Following the same fitting procedure as described above, we obtain the fitted values of energy barrier E_b, size λ, and critical force $f_c = 3E_b/\lambda$ in both the advancing and receding directions. All the data are well described by Eq. (11) and the final fitting results for different liquid samples are given in Table II. It is seen from Table II that the fitting results obtained from the capillary force relaxation are in good agreement with those from the rupture force spectroscopy. We also find from the fitting that the error bars associated with the rupture force spectroscopy are generally smaller than those associated the capillary force relaxation.

The above results thus demonstrate that the speed-dependent CFH and relaxation of capillary force for a suddenly stopped MCL are determined by the same microscopic mechanism and our model, as shown in Eqs. (8) and (11), captures the essential physics. The fact that two sets of the parameters E_b,λ, and f_0 are needed to describe the CL pinning (relaxation) and depinning dynamics in the advancing and receding directions, respectively, further support the composite model that the advancing and receding CLs are pinned by two different sets of relatively nonwetting and wetting defects on the fiber surface.

In deriving Eq. (8) [and Eq. (11)], we have assumed that the depinning force ΔF is a simple sum of N $(=(a/\lambda)\pi d)$ noninteracting defects of equal strength. While this is certainly an idealized assumption, we find the FTS-coated fiber has several unique features related to the assumption. First, as mentioned above, the FTS monolayer is known to be more uniform and closely packed than other self-assembled

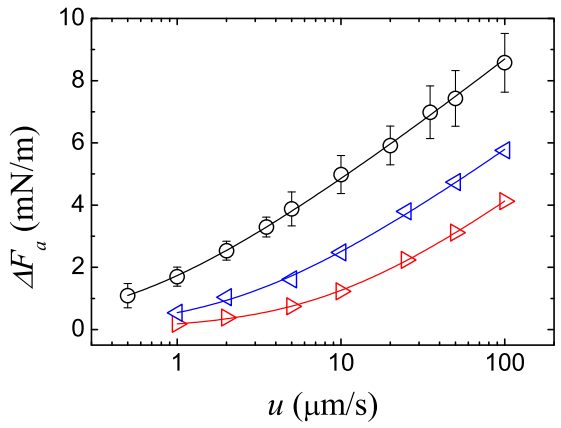

FIG. 9. Measured depinning force ΔF_a for the advancing CL as a function of fiber speed u for three liquid samples: water (black circles), octanol (blue left triangles), and hexanol (red right triangles). The error bars show the standard deviation of the measurements. The solid lines are the fits to Eq. (8).

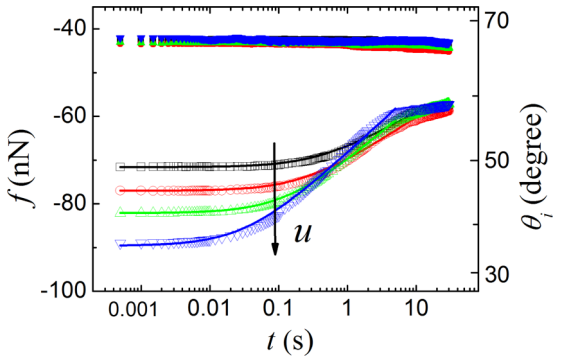

FIG. 10. Relaxation of the measured capillary force $f(t)$ and corresponding contact angle $\theta_i(t)$ as a function of time t after a MCL is suddenly stopped at $t = 0$. The measurements are made for the decane-air interface with different initial speeds: $u = 1$ μm/s (black), 2 μm/s (red), 5 μm/s (green), and 20 μm/s (blue). The upper four curves are obtained for the advancing CL and the lower four curves are obtained for the receding CL. The black long arrow points the direction of increasing u. The solid lines show the fits to Eq. (11).

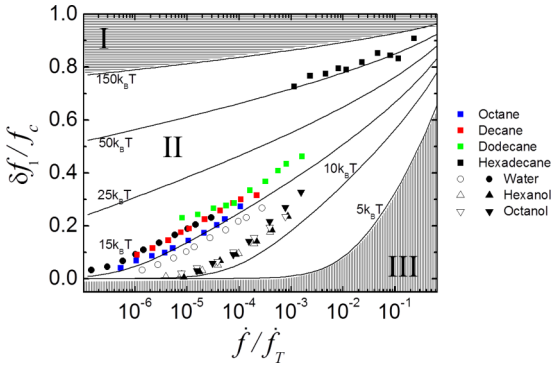

FIG. 11. Normalized mean rupture force per defect $\delta f_1/f_c$ as a function of the normalized pulling rate $\dot{f}_1/\dot{f}_T$ for different liquid samples. The solid symbols are obtained in the receding direction, and the open symbols are obtained in the advancing direction. The solid lines are given by Eq. (8) for $E_b = 5$, 10, 15, 25, 50, and 150 k_BT, respectively. The entire "phase diagram" may be divided into three regions (see text for more details): (I) strong pinning region (upper shaded area), (II) speed-dependent intermediate region (middle unshaded area), and (III) weak pinning region (lower shaded area).

monolayers on the silica substrate [35–37], and we have made efforts during the FTS coating to have a uniform coating with a minimum number of coating defects. This will reduce the overlapping effect between the defects. Second, because the CL is pinned primarily by a common type of defects in one direction, the depinning force ΔF is proportional to N rather than $\sqrt{N}$ [45]. Third, it is seen from Eq. (8) that the essential role of a/λ is to set a force scale for ΔF, and we find that the fitted values of E_b and λ are not very sensitive to the change of a. The error bar of E_b goes as $\ln(1 + \Delta a/a)k_BT$, where Δa is the deviation of a from its true value. Similarly, the error bar of λ goes as $(\Delta a/2a)\lambda$. Nevertheless, defects on an ambient solid surface do not have equal strength, which causes the fitted barrier parameters to be effective ones averaged over all the defects interacting with the CL. Our model is thus a first step toward the understanding of the microscopic origin of the CL interactions and dynamics. Further theoretical modeling is needed in order to fully describe more complex defect landscapes [24].

D. A unified "phase diagram" of CL depinning

With the measured ΔF_a and ΔF_r and the fitted values of E_b and λ, as well as the predetermined parameters a,k_s, and K_0, we now can present the depinning data from all of the liquid samples, as shown in Fig. 8, on a single unified "phase diagram". Following Eq. (8), we plot, in Fig. 11, the normalized mean rupture force per defect $\delta f_1/f_c$ as a function of the normalized pulling rate $\dot{f}/\dot{f}_T$ for all the liquid samples used in the experiment. The solid lines are given by Eq. (8) for five different values of E_b from 5 k_BT to 150 k_BT. The entire phase diagram may be divided into three regions. Region I is the strong pinning region with $E_b \gtrsim 150k_BT$, which is a typical energy associated with a single covalent bond of small molecules. CL pinning on a high-energy surface, such as a bare glass surface, belongs to this region. In this region, δf_1 shows large hysteresis with little u dependence and its value is close to f_c [18]. Without a strong u dependence, it is difficult to apply Eq. (8) to precisely determine E_b and λ.

Region III is the weak pinning region with $E_b \lesssim 5k_BT$, so that thermal fluctuations play a dominant role. In this region, $\delta f_1/f_c$ is very small (close to 0) and has little u dependence for small values of $\dot{f}/\dot{f}_T$ (up to $\sim 10^{-2}$). The measured f_i is close to $(f_0)_i$ [see Eq. (15)], and thus CFH is small in Region III. The measured capillary force for FC77, as shown in Fig. 6(d), belongs to this region. Only when the loading rate $\dot{f}/\dot{f}_T$ becomes very large ($> 10^{-2}$), $\delta f_1/f_c$ starts to show substantial u dependence. However, this fast loading rate is difficult to reach in the present experiment.

Region II is the speed-dependent intermediate region with $150k_BT \gtrsim E_b \gtrsim 5k_BT$. All the measured $\delta f_1/f_c$ for the seven liquid samples used in the present experiment (shown as symbols) lies in this region and shows strong u dependence. With the strong u dependence, one can use Eq. (8) to accurately determine the values of E_b and λ. It is seen from Fig. 11 that the measured $\delta f_1/f_c$ for most liquid samples varies in the range of 0.05–0.4. This result is close to our expectation, $\delta f_1/f_c \simeq 1/3$, based on the estimated defect energy [30] $E_b \simeq \lambda^2\gamma|\cos\theta_i - \cos(\theta_0)_i| \simeq \lambda\delta f_1$. Figure 11 thus reveals the essential physics of the rupture force spectroscopy of CL depinning and speed-dependent CFH.

E. CL pinning and depinning with varying solid-liquid interactions

We now examine how the energy barrier parameters E_b,λ, and f_c change with the solid-liquid interactions. This can be understood by rewriting Eq. (15) as

$$\Delta F_i = \gamma|\cos\theta_i - \cos(\theta_0)_i| = \Delta\gamma_{sv} - \Delta\gamma_{sl}, \qquad (16)$$

where $\Delta\gamma_{sv}$ is the change of the interfacial tension between the solid and vapor and $\Delta\gamma_{sl}$ is the change of the interfacial tension between the solid and liquid, both due to the defects on the solid surface. By using different liquids, $\Delta\gamma_{sv}$ does not change much, but $\Delta\gamma_{sl}$ changes considerably and so do the energy barrier E_b/k_BT and size λ.

1. *Energy barriers for different types of liquids*

As mentioned in Sec. III C, the eight liquid samples used in the experiment can be grouped into four different categories. FC77 is the first type of strong nonpolar liquid, whose molecular structure is similar to that of the FTS molecules grafted on the fiber surface. As a result, the interfacial tension (or energy) between the solid and liquid is the smallest among the eight liquids. The roughness of the defect landscape seems to have also been reduced accordingly. Indeed, there is little CFH for the FC77-air interface, and no measurable speed dependence is found for the measured capillary force in both the advancing and receding directions, as shown in Figs. 6 and 8(a).

Water is the second type of strong polar liquid, which has strong interactions with the FTS-coated fiber surface. As a result, their interfacial tension is the largest among the eight liquids used. The roughness of the defect landscape seems to have also been amplified accordingly. This strong solid-liquid interaction thus makes the water-air interface to be very

sensitive to both the wetting and nonwetting defects on the FTS-coated fiber surface. As shown in Figs. 8 and 9, water has the largest values of ΔF_r and ΔF_a among all the liquid samples studied here. It is found from Table II that the receding critical force $(f_c)_r \simeq 3(E_b)_r/\lambda_r$ for the water-air interface is about three times larger than that for the other liquid interfaces. As sketched in Fig. 4(b), the FTS-coated fiber surface has more wetting defects, which may be used to explain why the critical force $(f_c)_r$ for water in the receding direction is more than twice larger than $(f_c)_a$ in the advancing direction.

Between the two limiting types of liquids, alkanes are the third type of simple nonpolar liquids, and hexanol and octanol belong to the fourth type of primary alcohols, whose molecule size and surface tension are similar to those of the alkanes. The primary alcohols have an extra hydroxyl group at the end of the hydrocarbon chain, making them slightly polar than the alkanes. This hydroxyl group seems to enhance the interactions between the alcohol and surface defects, making the alcohol-air interface to be sensitive to both the wetting and nonwetting defects on the FTS-coated fiber surface. For the octanol-air interface, the values of E_b,λ, and f_c obtained in the receding direction are approximately the same as those obtained in the advancing direction. This symmetric behavior is also observed in the measured u dependence of CFH, as shown in Figs. 6(b), 8, and 9. The obtained values of E_b,λ, and f_c for hexanol are symmetric as well.

2. *Energy barrier for alkane chains with different carbon numbers*

Unlike the primary alcohols, which can sense the surface defects in both the advancing and receding directions, the interfacial tension between the alkanes and FTS-coated surface is further reduced. The interactions between the alkanes and surface defects seems to have also been reduced accordingly. As a result, the nonpolar alkanes cannot sense the weak (nonwetting) defects in the advancing direction anymore, and they can only sense the wetting holes, as sketched in Fig. 4(b), in the receding direction. In this case, the measured advancing contact angle θ_a will be very close to the equilibrium contact angle θ_0. As shown in Fig. 8(b), the u dependence of the measured ΔF_r for the alkanes becomes weaker with increasing carbon numbers from 8 (octane) to 16 (hexadecane). Correspondingly, the molecular size of the hydrocarbon chains is increased from $\sim$1 nm to $\sim$2 nm [46]. It is found from Table II that the obtained values of $(E_b)_r$ and λ_r increase continuously with the molecular size of the hydrocarbon chains. This effect can be understood by considering the physical matching of the liquid molecules to the size of the defects. The liquid molecules will not be able to effectively sense those defects whose size is smaller than the liquid molecules. As a result, the obtained defect size λ_r increases with the size of the hydrocarbon chains. The fitted values of $(E_b)_r$ and λ_r for hexadecane are found to be much larger than those for the other alkanes. Figure 11 also shows a large jump in the measured $\delta f_1/f_c$ for hexadecane. At the moment, we do not know exactly what causes the large change in $\delta f_1/f_c$. We suspect that such a large jump in $(E_b)_r$ and λ_r may be related to the formation of a crystallized monolayer at the hexadecane-air interface [47], which will significantly change the solid-liquid interaction at the CL.

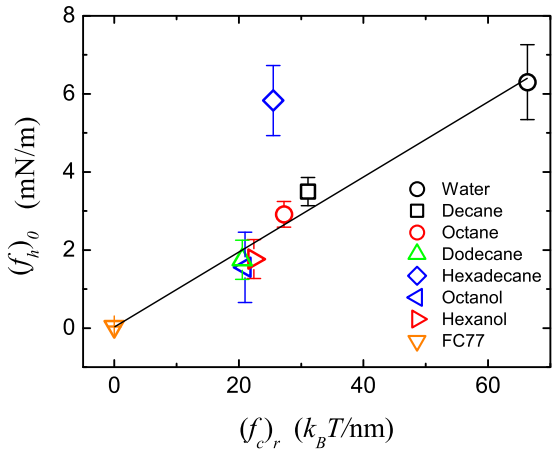

FIG. 12. Measured hysteresis force $(f_h)_0$ as a function of the receding critical force $(f_c)_r$ for eight liquid samples: water (black circle), decane (black square), octane (red circle), dodecane (green up triangle), hexadecane (blue diamond), octanol (blue left triangle), hexanol (red right triangle), and FC77 (orange down triangle). The error bars show the standard deviation of the force measurements. The solid line is a linear fit to the data points (excluding the blue diamond): $(f_h)_0 = b(f_c)_r$ with $b = 23.1/\mu$m.

Finally, we discuss how the asymptotic values, $(f_0)_r$ and $(f_0)_a$, vary with different liquids. Figure 12 shows the measured asymptotic value of the hysteresis force $(f_h)_0$ as a function of the receding critical force $(f_c)_r$ for the eight liquid samples. Here $(f_h)_0$ is defined as $(f_h)_0 = |(f_0)_a - (f_0)_r|/\pi d$, which represents the hysteresis force per unit length at the limit $u \to 0$. The receding critical force $(f_c)_r$ is used here to indicate the intrinsic rapture force for a single defect on the FTS-coated fiber surface. Except for hexadecane, all the data points can be well described by a linear function $(f_h)_0 = b(f_c)_r$ (solid line), from which we obtain the slope $b = 23.1/\mu$m. Physically, b represents the line density of those defects with large pinning barriers, which prevent the CL from further relaxing to a global minimum energy state. This value of b is approximately 15% of the obtained line density of total defects on the fiber surface $a/\lambda \simeq 0.3/2$ nm $= 150/\mu$m. The results shown in Fig. 12 thus are consistent with those shown in Table II.

VI. CONCLUSION

We have carried out systematic AFM measurements of capillary force hysteresis (CFH) and relaxation of a circular moving contact line (MCL) formed on a long micron-sized hydrophobic fiber intersecting a liquid-air interface. Eight different liquid-air interfaces are used, and each interface shows its own characteristic CFH and MCL relaxation. An important feature shown in Figs. 5–7 is that the speed-dependent CFH is uniquely connected to the MCL relaxation, which allows us to conduct a simultaneous experimental study of both processes. An unified model based on force-assisted barrier crossing is developed to determine the underlying energy barrier E_b and size λ associated with the surface defects. With this theoretical framework, we provide a common understanding about the microscopic origin of the observed asymmetric

speed-dependent CFH and slow relaxation of a suddenly stopped MCL. It is shown that the advancing and receding CLs are influenced by two different sets of relatively wetting and nonwetting defects on the surface. These two different types of defect landscapes give rise to an asymmetric speed dependence of CFH and two different metastable (pinned) states for MCL relaxation.

By systematically varying the solid-liquid interactions with different liquid samples, we find a universal behavior of the speed-dependent CFH and CL relaxation, which is summarized in Figs. 8 and 9 and in Table II. The energy barrier associated with the defects on the same FTS-coated surface is found to be affected not only by the solid-liquid interfacial tension, which sets the overall energy scale of the interactions, but also by the detailed chemical interactions between the liquid and surface defects. As shown in Fig. 11, the CL depinning dynamics can be quantitatively understood with a unified "phase diagram," which involves solid-liquid interactions in three different regions: (1) strong pinning region, (2) speed-dependent intermediate region, and (3) weak pinning region. The experiment demonstrates that the rupture force spectroscopy of CL depinning and capillary force relaxation spectroscopy are powerful tools, which open the door to a wide variety of new experiments using a fiber surface with controlled patterns or micro-textures to study the CL dynamics.

ACKNOWLEDGMENTS

We thank H.-Y. Chen, T.-Z. Qian, and X.-G. Ma for illuminating discussions. This work was supported in part by RGC of Hong Kong SAR under Grant Nos. A-HKUST616/14-A (P.T.) and C6004-14G (P.T.) and by Agence Nationale de la Recherche under Grant No. ANR-14-CE05-0017-02 (E.C.).

[1] P.-G. de Gennes, Rev. Mod. Phys. **57**, 827 (1985).
[2] L. Leger and J.-F. Joanny, Rep. Prog. Phys. **55**, 431 (1992).
[3] E. L. Decker and S. Garoff, J. Adhesion **63**, 159 (1997).
[4] D. Bonn, J. Eggers, J. Indekeu, J. Meunier, and E. Rolley, Rev. Mod. Phys. **81**, 739 (2009).
[5] J. H. Snoeijer and B. Andreotti, Annu. Rev. Fluid Mech. **45**, 269 (2013).
[6] E. B. V. Dussan and S. H. J. Davis, Fluid Mech. **65**, 71 (1974).
[7] D. Quéré, Annu. Rev. Mater. Res. **38**, 71 (2008).
[8] M. Ramiasa, J. Ralston, R. Fetzer, and R. Sedev, Adv. Colloid Interface Sci. **206**, 275 (2014).
[9] J. M. Di Meglio, Europhys. Lett. **17**, 607 (1992).
[10] G. D. Nadkarni and S. Garoff, Europhys. Lett. **20**, 523 (1992).
[11] A. Paterson, M. Fermigier, P. Jenffer, and L. Limat, Phys. Rev. E **51**, 1291 (1995).
[12] S. Moulinet, A. Rosso, W. Krauth, and E. Rolley, Phys. Rev. E **69**, 035103(R) (2004).
[13] C. Priest, R. Sedev, and J. Ralston, Phys. Rev. Lett. **99**, 026103 (2007).
[14] M. Reyssat and D. Quéré, J. Phys. Chem. B **113**, 3906 (2009).
[15] S. M. M. Ramos, E. Charlaix, A. Benyagoub, and M. Toulemonde, Phys. Rev. E **67**, 031604 (2003).
[16] S. Ramos and A. Tanguy, Eur. Phys. J. E **19**, 433 (2006).
[17] M. Delmas, M. Monthioux, and T. Ondarcuhu, Phys. Rev. Lett. **106**, 136102 (2011).
[18] Y. J. Wang, S. Guo, H.-Y. Chen, and P. Tong, Phys. Rev. E **93**, 052802 (2016).
[19] X.-M. Xiong, S. Guo, Z.-L. Xu, P. Sheng, and P. Tong, Phys. Rev. E **80**, 061604 (2009).
[20] J.-M. Di Meglio and D. Quéré, Europhys. Lett. **11**, 163 (1990).
[21] M. M. Yazdanpanah, M. Hosseini, S. Pabba, S. M. Berry, V. V. Dobrokhotov, A. Safir, R. S. Keynton, and R. W. Cohn, Langmuir **24**, 13753 (2008).
[22] J. D. de Baubigny, M. Benzaquen, L. Fabié, M. Delmas, J.-P. Aime, M. Legros, and T. Ondarçuhu, Langmuir **31**, 9790 (2015).
[23] D. Guan, Y. J. Wang, E. Charlaix, and P. Tong, Phys. Rev. Lett. **116**, 066102 (2016) and Supplemental Information.
[24] E. Evans, Annu. Rev. Biophys. Biomol. Struct. **30**, 105 (2001).
[25] H. J. Lin, H. Y. Chen, Y. J. Sheng, and H. K. Tsao, Phys. Rev. Lett. **98**, 088304 (2007).
[26] R. W. Friddle, Phys. Rev. Lett. **100**, 138302 (2008).
[27] A. Garg, Phys. Rev. B **51**, 15592 (1995).
[28] X.-G. Ma, P.-Y. Lai, B. J. Ackerson, and P. Tong, Soft Matter **11**, 1182 (2015).
[29] A. Prevost, E. Rolley, and C. Guthmann, Phys. Rev. Lett. **83**, 348 (1999).
[30] E. Rolley and C. Guthmann, Phys. Rev. Lett. **98**, 166105 (2007).
[31] G. I. Bell, Science **200**, 618 (1978).
[32] S. Guo, X.-M. Xiong, Z.-L. Xu, P. Sheng, and P. Tong, Chin. Phys. B **23**, 116802 (2014).
[33] P. Silberzan, L. Leger, D. Ausserre, and J. J. Benattar, Langmuir **7**, 1647 (1991).
[34] J. B. Brzoska, I. B. Azouz, and F. Rondelez, Langmuir **10**, 4367 (1994).
[35] Y.-X. Zhuang, O. Hansen, T. Knieling, C. Wang, P. Rombach, W. Lang, W. Benecke, M. Kehlenbeck, and J. Koblitz, J. Micromech. Microeng. **16**, 2259 (2006).
[36] O. P. Khatri, D. Devaprakasam, and S. K. Biswas, Tribol. Lett. **20**, 235 (2005).
[37] W. R. Ashurst, C. Carraro, and R. Maboudian, IEEE Trans. Devices Mater. Rel. **3**, 173 (2003).
[38] T. M. Mayer, M. P. de Boer, N. D. Shinn, P. J. Clews, and T. A. Michalske, J. Vac. Sci. Technol. B **18**, 2433 (2000).
[39] J. L. Hutter and J. Bechhoefer, Rev. Sci. Instrum. **64**, 1868 (1993).
[40] L.-H. Tang, in *Encyclopedia of Complexity and Systems Science*, edited by R. A. Meyers (Springer, New York, 2009).
[41] P. Le Doussal and K. J. Wiese, Phys. Rev. E **82**, 011108 (2010).
[42] S. Guo, M. Gao, X.-M. Xiong, Y. J. Wang, X.-P. Wang, P. Sheng, and P. Tong, Phys. Rev. Lett. **111**, 026101 (2013).
[43] S. Guo, C. H. Lee, P. Sheng, and P. Tong, Phys. Rev. E **91**, 012404 (2015).
[44] D. M. Kaz, R. McGorty, M. Mani, M. P. Brenner, and V. N. Manoharan, Nat. Mater. **11**, 138 (2012).
[45] M. O. Robbins and J. F. Joanny, Europhys. Lett. **3**, 729 (1987).
[46] L. S. Bartell, J. Am. Chem. Soc. **81**, 3497 (1959).
[47] T. K. Xia and U. Landman, Phys. Rev. B **48**, 11313 (1993).